

Combining Google Traffic Map with Deep Learning Model to Predict Street-Level Traffic-Related Air Pollutants in a Complex Urban Environment

Peng Wei^{1,2}, Song Hao^{3*}, Yuan Shi^{4*}, Abhishek Anand⁵, Ya Wang², Mengyuan Chu², Zhi Ning^{2*}

1 College of Geography and Environment, Shandong Normal University, Jinan, China

2 Division of Environment and Sustainability, The Hong Kong University of Science and Technology, Hong Kong, China

3 State Key Laboratory of Information Engineering in Surveying, Mapping and Remote Sensing, Wuhan University, Wuhan, China

4 Department of Geography & Planning, University of Liverpool, Liverpool, UK

5 Department of Mechanical Engineering, Carnegie Mellon University

*Email: whusong@whu.edu.cn, yuan.shi@liverpool.ac.uk, zhining@ust.hk

Highlights:

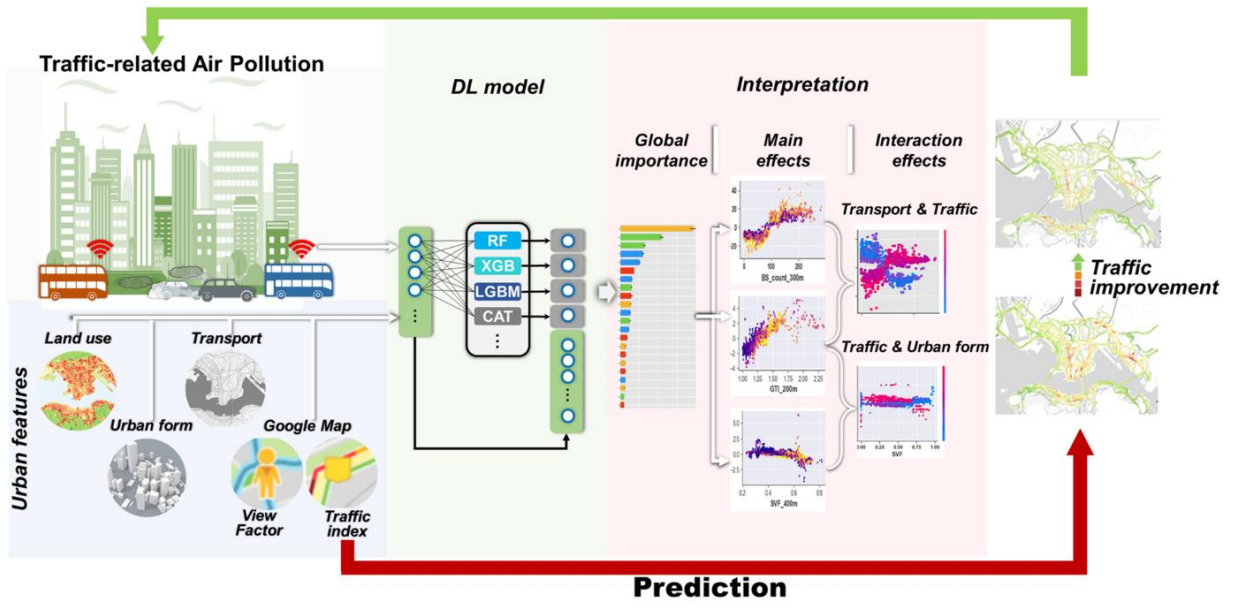
1. Real-time traffic congestion extraction method serving as a crucial proxy for estimating traffic-related air pollution (TRAP).
2. Deep learning model superiority demonstrated higher accuracy and predictive capabilities compared to traditional machine learning models.
3. Model-agnostic interpretation quantifying individual feature contributions and decoupling feature interactions.
4. Assessment of traffic-congestion induced pollution demonstrating the effectiveness of targeted TRAP control strategies.

Abstract

1 Background: Traffic-related air pollution (TRAP) is a major contributor to urban pollution and
2 varies sharply at the street level, posing a challenge for air quality modeling. Traditional land
3 use regression models combined with data from fixed monitoring stations may be unable to
4 predict and characterize fine-scale TRAP, especially in complex urban environments influenced
5 by various features. This study aims to estimate fine-scale (50 m) concentrations of nitrogen
6 oxides (NO and NO₂) in Hong Kong using a deep learning (DL) structured model.
7 Methods: We collected data from mobile air quality sensors on buses and crowd-sourced
8 Google real-time traffic status as a proxy for real-time traffic emissions. Our DL model was
9 compared with existing machine learning models to assess performance improvements. Using
10 an interpretable machine learning method, we hierarchically evaluated the global, local, and
11 interaction effects for different features.
12 Results: Our DL model outperformed existing machine learning models, achieving R² values
13 of 0.72 for NO and 0.69 for NO₂. The incorporation of traffic status as a key predictor improved
14 model performance by 9% to 17%. The interpretable machine learning method revealed the
15 importance of traffic-related features and their pairwise interactions.
16 Conclusion: The results indicate that traffic-related features significantly contribute to TRAP
17 and provide insights and guidance for urban planning. By incorporating crowd-sourced Google
18 traffic information, we assessed traffic abatement scenarios that could inform targeted strategies
19 for improving urban air quality.

Keywords: machine learning, deep learning, mobile measurement, street-level pollution, air quality sensor, crowd-sourced

Abatement



20 1 INTRODUCTION

21 Traffic-related air pollution (TRAP) produced by the emission of motor vehicles is a major
22 contributor to urban air pollution (Grange et al., 2017; Guarnieri and Balmes, 2014; Harrison
23 et al., 2021), including nitric oxide (NO), nitrogen dioxide (NO₂), black carbon (BC), VOCs
24 (Volatile Organic Compounds) and particulate matter. Evidence is mounting that long-term
25 exposure to TRAP is linked to several adverse health outcomes, such as cardiovascular disease,
26 respiratory symptoms and asthma (Ji et al., 2024; Zhu et al., 2023), premature mortality and
27 dementia (Chen et al., 2017; HEI, 2010; World Health Organization, 2016), especially for
28 vulnerable groups living in proximity to or at busy streets (Hoek et al., 2002; Kim et al., 2004).
29 In urban areas, most people who live within 500 m away from major roads suffer from the
30 health effects of long-term or short-term exposure to air pollution (Delfino et al., 2008; Su et
31 al., 2015). Governments and environmental agencies deploy in-situ regulatory stations to
32 monitor the air quality and establish regulations with guidelines or standards. Limited by the
33 high cost and maintenance, conventional fixed-site monitoring stations are often sparsely
34 distributed that cannot capture spatial variations of pollutants at fine scales(Kumar et al., 2015).

35 Mobile measurements provide an alternate way to capture pollutant variations at sub-kilometer
36 scales in urban environments(Apte et al., 2017; Hatzopoulou et al., 2012). To estimate fine-
37 grained spatial variation of pollutants concentrations, several mobile sampling strategies
38 coupled with empirical land use regression (LUR) models have been developed and
39 demonstrated the capacity to quantify human exposure(C. Simon et al., 2018; Dalgleish et al.,
40 2018; Deville Cavellin et al., 2015; Hankey et al., 2019; Hankey and D. Marshall, 2015; Shi et
41 al., 2016). Recently, rapid advances in internet of things (IOT) technologies and low-cost air
42 quality sensors have extended the scope of air quality measurement in multiple settings (Kumar
43 et al., 2015; Mead et al., 2013; Thompson, 2016). Data quality from these sensor-based
44 measurements is enhanced by evolving calibration paradigms and hardware designs (Baron and
45 Saffell, 2017; Kumar et al., 2015; Morawska et al., 2018). These low-cost air quality sensors
46 can be deployed in varied scenarios to expand existing monitoring networks or mobile
47 campaigns in complex urban environments (Hatzopoulou et al., 2017; Morawska et al., 2018).

48 The LUR model aims to estimate air pollutant concentrations and assess individual exposure
49 levels in epidemiological studies (Briggs, 2006; Hoek et al., 2008a). It utilizes geographic
50 covariates as spatial predictors, e.g., land use types, traffic and transport infrastructures
51 (Dalgleish et al., 2018; Hoek et al., 2008a). Linear relationships in the LUR model may
52 overlook complex nonlinearities between air pollutant concentrations and predictors. Machine
53 Learning (ML) based air quality models, such as artificial neural network (ANN), random forest
54 (RF), and XGBoost, offer improved accuracy and resistance to multicollinearity compared to
55 linear regression models (Di et al., 2016; Ding et al., 2021; Hu et al., 2017; Li et al., 2017; Xiao
56 et al., 2018; Zhou et al., 2021; Ding et al., 2021; Xiao et al., 2018; Zhou et al., 2021). On the
57 other hand, deep learning (DL) models have gained attention for extracting complex features in
58 hierarchical representations for air pollution prediction (Lyu et al., 2019; Pak et al., 2020; Yan
59 et al., 2020). Meanwhile, ensemble strategies integrate multiple base models in air pollution

60 modeling, combining their advantages for improved predictions (Di et al., 2019; Xiao et al.,
61 2018). Still, the complexity improves ML model's performance at the cost of the interpretability,
62 to open the "black box" of the ML model and make it understandable is necessary to extend the
63 insight of feature effects and interactions (Molnar et al., 2020; Reichstein et al., 2019; Zhong et
64 al., 2021).

65 Traditional tabular predictors have limitations in representing fine-scale spatial variations of
66 traffic emissions and dynamic transportation developments. Nontabular data enriched with
67 detailed street-level air quality information can greatly contribute to air quality assessments
68 when synchronized with mobile sensor measurements (Wang et al., 2023). The hybrid models
69 incorporate outputs from dispersion as input for traffic emission simulation or as new data
70 sources which enhanced the spatial predictability of the models (Gerges et al., 2024; Lloyd et
71 al., 2023). Google Maps provides an array of non-tabular data, accessible as graphical
72 information, while Google Street View (GSV) amasses a vast collection of panoramic imagery
73 (Gong et al., 2018). Combined with deep learning models, GSV has been widely used to
74 quantify urban characteristics and predictors (Gong et al., 2018; Hu et al., 2020; Li and Ratti,
75 2019). Meanwhile, Google Maps has used "crowd-sensed" data from phone users to analyze
76 and predict real-time traffic congestion conditions (Google Maps, 2009; Nair et al., 2019).
77 Compared with static traffic data, real-time traffic congestion status can supply more dynamic
78 and up-to-date traffic information that is associated with transient vehicle emissions and can
79 better indicate short-lived pollutants, such as NO_x, UFP and BC (Hilpert et al., 2019). Quantify
80 and understand congestion-induced TRAP enables policymakers to make more informed
81 decisions and targeting effective interventions to reduce exposure levels (Gately et al., 2017).
82 Nevertheless, a robust modeling framework that integrates traffic congestion data and providing
83 interpretable results in complex urban environments yet to be explored.

84 In this study, we employed low-cost sensors on fixed-route buses to measure NO and NO₂
85 across varied road environments in Hong Kong and built high performance model to estimate
86 street-level TRAP. We introduced Google traffic congestion status as a predictor to estimate
87 TRAP in the complex urban environment. Furthermore, we use model-agnostic strategies to
88 quantify feature contributions and get a thorough understanding of the complex interactions
89 between different variables that influence on TRAP. Finally, by evaluating the congestion
90 influence on street-level pollution, we highlighted the importance of traffic improvement on
91 TRAP abatement in key localized roads.

92 **2 MATERIALS AND METHODS**

93 **2.1 Study Area and Air Pollution Measurement**

94 Hong Kong's urban area is among the densest in the world's mega-cities. Over 7.5 million
95 residents inhabit approximately 262 km² of developed land. Hong Kong has over 10,000 high-
96 rise buildings (>40 meters) (Emporis, 2018) and residential densities exceeding 110,000
97 people/km² (Figure S1). The study area encompasses Kowloon Peninsula and Hong Kong
98 Island's ultra-dense urban buildings and road networks (Figure S2). In this region, the high

99 building height-to-street width ratio creates deep street canyons. Narrow streets often collocated
100 with high level of traffic congestion, exacerbating air pollution further. The mobile sensor
101 measurements were deployed on double-deck buses that travel along fixed routes to capture
102 repeat measurements during bus schedule hours. The monitoring campaign was conducted over
103 the course of two months in 2017, specifically in April and July, aligning with the spring and
104 summer seasons respectively in Hong Kong. This seasonal timing was chosen to assess
105 environmental variations across different climatic conditions. NO and NO₂ were measured by
106 electrochemical gas sensors with a sampling rate of 5 seconds. Details on the platform, sensor
107 calibration, and data quality control are in our previous work (Wei et al., 2021) and Text S1. In
108 the study area, ten selected bus routes covered multiple road types and environments. Figure
109 S3 represents the mobile measurement routes and the percentage of road types in the study area.
110 The Hong Kong road network was segmented into equal lengths, and all measurements were
111 allocated to the nearest road segments. The mobile measurements campaign covered 130 km,
112 and a total length of 100 km was selected with a repeat measurement number of more than 20
113 times (about 2000 road segments). We chose 50 m resolution to balance the representativeness
114 of the measurement and route repeat numbers (Figure S4). All measurements were allocated to
115 road segments for further model building (Dalgleish et al., 2018; J. Miller et al., 2020). First, we
116 assigned the mean concentration for each session of unique drive pass to its corresponding road
117 segment. Then, we calculated the median of these drive pass mean concentration values for
118 each road segment. This median concentration was used to represent the typical level of
119 pollution on that road segment. To ensure the representativeness of measurements, we excluded
120 road segments that were visited fewer than 20 times (Hatzopoulou et al., 2017). As a comparison,
121 we also used grid based geo-processing method to reconstruct measurements and variables (Shi
122 et al., 2016). Meanwhile, we followed Apte's steps that used multiplicative time-of-day factor
123 to correct diurnal background variation (Apte et al., 2017). The adjustment factor was based on
124 Hong Kong Environmental Protection Department (HKEPD) roadside air quality station. The
125 influence of meteorological conditions was assessed (wind speed and direction) for individual
126 routes at the microscale (50m). The result revealed non-significant p-values (>0.05) for most
127 routes, indicating that wind speed and direction did not exert a dominant influence on NO and
128 NO₂ concentrations compared to traffic-related features. Detailed statistical results are provided
129 in the supplementary materials (Table S1).

130 **2.2 Geo-Predictor Variables and Processing**

131 Based on previous LUR model building (Hoek et al., 2008b; Su et al., 2009), we collected four
132 types of traditional spatial predictors to characterize traffic-related emission intensity: transport
133 infrastructure, land use types, and population. The land use variables cannot fully represent
134 Hong Kong's high-density and variation of urban building morphology compared with low-
135 density urban environment. We followed our previous work which used urban morphology
136 features to characterize Hong Kong's unique urban environment (Shi et al., 2016). All variables
137 and summaries are listed in Table S2 with detailed information. We used road segment centroid
138 variables and different buffer sizes to generate candidate variables (353 in total) for models.

139 **2.3 Google Map Predictors**

140 Google maps platform (GMP) allows users to use an application program interface (API) to
141 connect the platform and extract information. We selected two modes of GMP free data as
142 predictors.

143 **2.3.1 Google Street View Factor**

144 For each road segment, we collected centroid panorama images via API key to access
145 corresponding GSV ID and download each tile image. Afterward, all tiles were combined to
146 generate a panorama image. The GSV images collected in the same year (2017) were collected
147 to match the mobile measurement. We used a scene parsing based deep learning model to parse
148 an image into varied semantic categories and extract street-level features (Text S3, Figure S5)
149 (Zhao et al., 2017). Considering Hong Kong's unique urban morphology with narrow streets
150 forming a street canyon environment, we reproject the segregated panorama images onto a
151 circular plane and generate a fisheye image based photographic method instead of the plane
152 percentage calculation (Li et al., 2018). Detailed information and calculation equations are
153 elaborated in Text S3. The view factors (VFs) of the sky (SVF), building (BVF) and trees (TVF)
154 were selected as candidate predictors covering approximately 95% of street view in the study
155 area. We averaged the VFs of two years (2017 and 2018) to decrease the influence of sunshine
156 on segmentation in the high-rising areas and used the buffered areas of VFs as candidate
157 predictors.

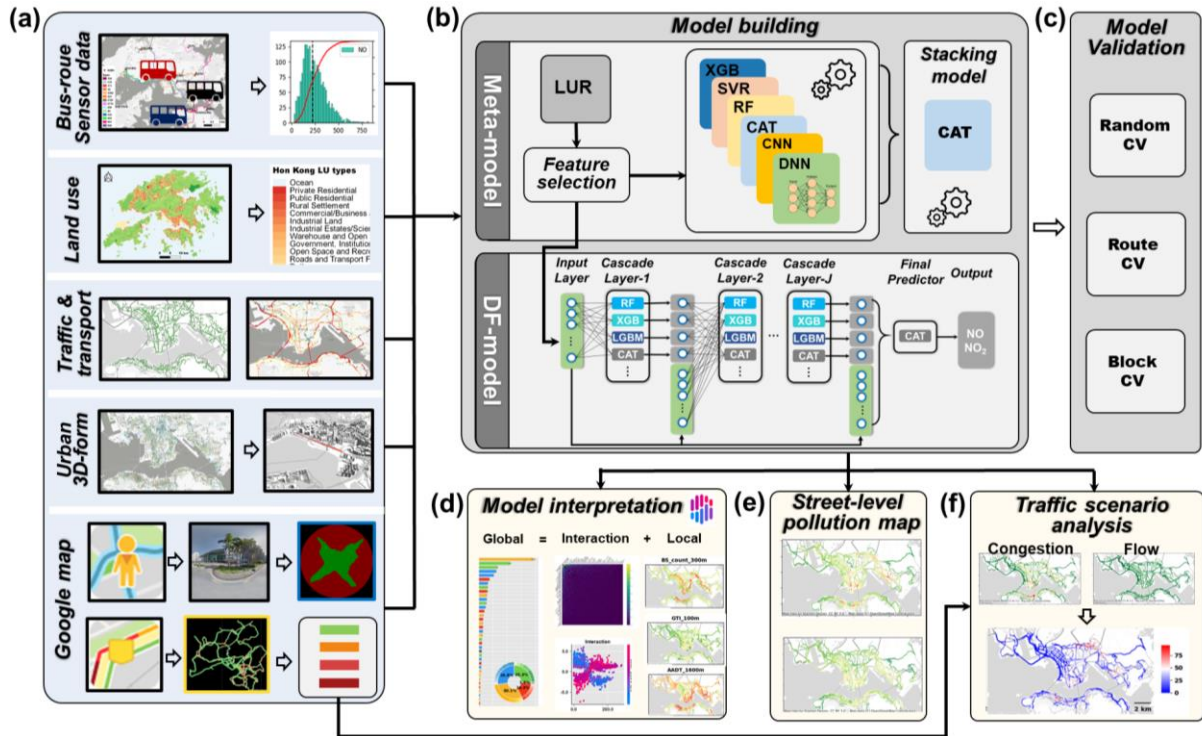
158 **2.3.2 Real-Time Google Traffic Index (GTI)**

159 Google Maps display real-time traffic status with a color-coded system that overlays on the
160 base map with multiple map elements. We used GMP to create a traffic status-only layer via
161 API, extracting traffic data from Google Maps. The redesigned map is saved as time-labeled
162 images during mobile measurements. An image processing and identification algorithm was
163 developed to pick up traffic status (Figure S6). We define Google traffic index (GTI) ranged
164 from 1 to 4 to indicate the congestion status (Table S3). Finally, each road segment was assigned
165 with GTI that correspond to the mobile measurements time. We sampled traffic map at a 3
166 minute interval and synchronized with the mobile measurement campaign time. The detailed
167 steps for traffic status image identification and road network map fusion are explained in Text
168 S4. The on-road traffic congestion status GTI and buffered GTI which represent neighborhood
169 congestion status influences were calculated as candidate predictors. Meanwhile, the GTI was
170 also integrated with traffic volume to represent the influence of vehicle fleet traffic status on-
171 road pollution. Accordingly, the traffic index in synchronization with bus GPS speed was
172 converted into real vehicle fleet speed for different types of roads (Table S4).

173 **2.4 Model Building**

174 We built four types of prediction models to assess their performance: the basic LUR model was
175 developed as a benchmark model and feature selection, machine learning models, multi-layered

176 deep learning models and an ensemble model which utilized different single models as base
 177 estimators (Figure 1). It should be noted that the fundamental unit of analysis and prediction is
 178 the road segment at a resolution of 50 meters, tailored for assessing the on-road ambient
 179 environment.



180
 181 Figure 1 The framework of the model building and applications in this study. (a) Data parts, (b) model building,
 182 (c) model CV strategies, (d) model interpretation, (e) prediction and (f) scenario analysis.

183 2.4.1 LUR Model Building

184 We performed a two-step strategy on the basic LUR model building. Firstly, we used a distance-
 185 decay regression selection strategy (ADDRESS)(Shi et al., 2016; Su et al., 2009) to screen
 186 candidate variables (both on-road and buffered variables) as model inputs for the second step
 187 and other models. For each type of variable, only variables with the highest correlation
 188 coefficient with the target pollutant were selected as model input. This step can avoid
 189 multicollinearity between different buffer size variables(Shi et al., 2016). Secondly, a forward
 190 selection procedure was conducted by starting with the variable that had the highest adjusted
 191 R^2 . The variables that increased the model adjusted R^2 by more than 0.01 and reduced the model
 192 residual error were retained. The model building process was terminated when a variable is not
 193 significant ($p < 0.1$) to the model or the variance inflation factor (VIF) exceeded 5 (Hankey et
 194 al., 2017).

195 2.4.2 Machine Learning (ML) Models

196 We applied five supervised ML models to estimate street-level air pollution and compare their
 197 performance: support vector regression (SVR), random forest (RF), light gradient boosting
 198 Machine (LGBM), extreme gradient boosting (XGB), CatBoost (CAT). Detailed explanations

199 of the stacking model building and structure can be found in Text S5 and Figure S8. RF is a
200 bagging method which integrating multiple decision trees with each node of the tree is split
201 according to the best of a subset of randomly predictors. Unlike RF, GBDT used boosting
202 method by sequentially connected decision trees to obtain a strong learner. XGB was developed
203 based on GBDT and evolved by adding regularization term which reduced model complexity
204 and accelerated solution process. CAT is also a gradient boosting on decision trees-based
205 framework that utilizes a boosting method that is well-suited for classification or regression
206 tasks that involve categorical and heterogeneous datasets (Hancock and Khoshgoftaar, 2020).
207 The development of CAT occurred more recently compared to other models, and it has
208 demonstrated a growing potential in recent times (Ding et al., 2021; Zhou et al., 2021). For all
209 ML models training stages, the hyperparameters were tuned with a grid-search method and are
210 listed in Table S5. We employed a stacking method that learns from the prediction results of
211 several base ML models and used a meta-model for the final prediction. The stacking strategy
212 could utilize advantage of different models performance that varied at spatial and
213 outperformance than single model. The base ML models were developed and CAT was chosen
214 for the meta-model. The stacking method can be extended to multiple layers, thus we built a 2-
215 layer and 3-layer structured model to evaluate model performances.

216 **2.4.3 Deep Learning (DL) Models**

217 We used a deep neural network (DNN) model and a modified convolutional neural networks
218 (CNN) model, ResNet, for our regression prediction task. ResNet often contains deep hidden
219 layers in the network and shows high performance for image recognition works. We modified
220 ResNet model for regression task by replaced convolutional layers and pooling layers with fully
221 connected layers in the residual block (Figure S9) (Chen et al., 2020). The DL models were
222 optimized with searching layers and hyperparameters (Table S5).

223 Deep forest (DF) model is a deep learning structured model and used multiple ensemble base
224 models to replace neurons in the hidden layer (Zhou and Feng, 2019), in other words, DF
225 combines DL structure and stacking strategy. The base learners contain RF and extreme trees
226 (ET) which constituted hidden layers. The ADDRESS selected features were as input for best
227 models (ranking by performance) in the cascade layer, the prediction result was concatenated
228 with raw input features as augment features and as input for the next layer (Figure 1(b)). DF
229 model training process will terminate if there is no significant performance gain. For each
230 hidden layer, a cross validation (CV) was carried out to avoid overfitting. Finally, a meta-
231 predictor is connected to the augmented outputs by the last hidden layer which produce the final
232 prediction results. In this study, we used DF model structure and built-in base models were
233 replaced with optimized base models developed in Section 2.4.2 to serve as estimators and
234 predictors.

235 **2.5 Model-Agnostic Interpretation**

236 We employed a model-agnostic (compared to model-specific) interpretation method for “black-
237 box” ML and DL models (Figure 1(d)), which enables us to compare multiple ML models

238 flexibly (Molnar, 2019; Molnar et al., 2020). The SHapley Additive exPlanations (SHAP) is a
239 model-agnostic interpretation technique that calculates feature importance using Shapley values,
240 which are grounded in game theory (Lundberg and Lee, 2017). SHAP values provide a unified
241 approach for explaining model results through local explanations based on the concept of
242 additive feature attribution. By summing the marginal contributions of all instances, SHAP
243 values can evaluate global feature importance. Unlike built-in feature importance for special
244 models which only show a global feature characteristic, SHAP values provide local
245 interpretability, enabling a detailed examination of each individual instance. Additionally,
246 SHAP can also generalize feature interaction effects instead of assuming that features are
247 mutually independent. Text S6 gives a detailed description of SHAP values of global and local
248 interpretations and interaction effects calculation.

249 **2.6 Model Evaluation and Predictions**

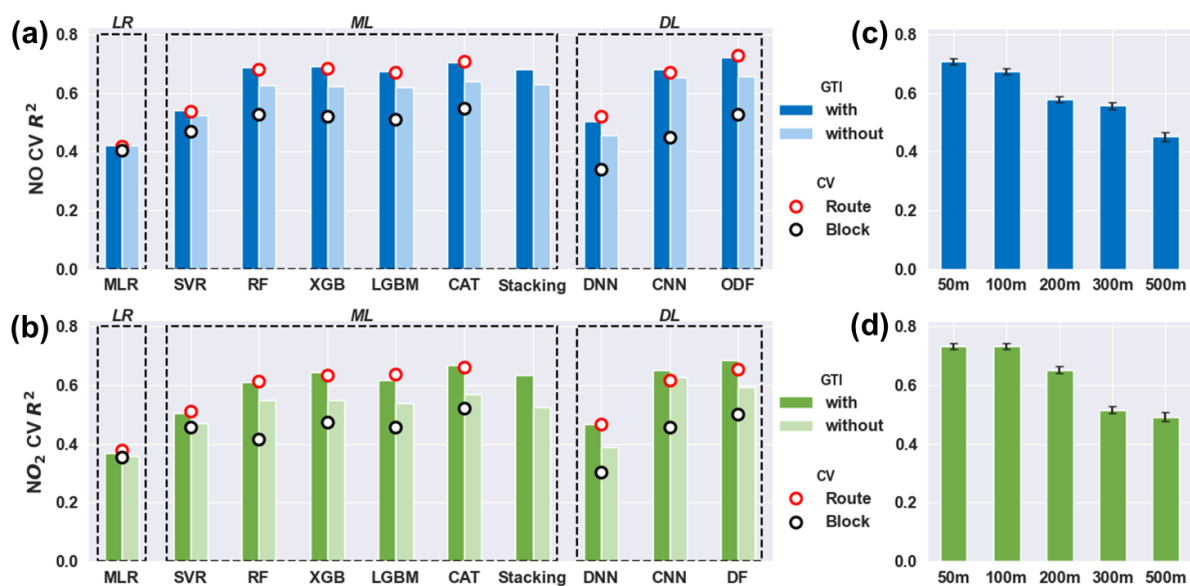
250 The model performance was evaluated by adjusted R^2 , root-mean-square-error (RMSE), and 5-
251 fold cross-validation (CV). Apart from random split CV, we designed route-based CV and
252 spatial block CV evaluation strategies (Figure 1(c)) to assess model prediction robustness (Text
253 S7, Figure S9). For the segment-based prediction, we calculated the required predictors for each
254 road segment centroid to estimate NO and NO₂ concentrations with the optimal DF model
255 (Figure 1(e)).

256 Further, leveraging the Google traffic data, we designed a counterfactual scenario (Figure 1(f))
257 to probe the impact of traffic status transition from real-world to congestion-free status on road
258 pollution. Two types of strategies were considered: first, a predictive comparative analysis (or
259 what-if) analysis to simulate potential effects of transitioning from congestion to a free status,
260 and second, a causal analysis employing a nonlinear Double Machine Learning (DML) to
261 estimate average causal effects of these changes, more details can be found in Text S8.

262 **3 RESULTS**

263 **3.1 Mobile Measurements and Model Performance**

264 The statistic of mobile measurements and corresponding co-variables are shown in Figure S10.
265 The median concentrations of on-road NO, NO₂ are 250 ppb and 40 ppb, respectively, which
266 present skewed distributions indicating high concentration segments and spatial heterogeneity.
267 The on-road TRAP revealed high levels of pollution and spatial variations (Figure S11), similar
268 findings could be found in previous studies that were conducted in Hong Kong and many other
269 Chinese megacities (Lee et al., 2017; Li et al., 2019). Such ambient pollution levels were
270 manifold of those from mobile campaigns deployed in the U.S and European countries (Apte
271 et al., 2017).



272
 273 Figure 2 Model performance of R^2 for NO (a) and NO₂ (b). The red dots are bus-route CV, and black dots are
 274 spatial block CV. The light bars are the model performance without GTI related variables (the stacking model only
 275 supported random CV). The spatial resolution performance for NO (c) and NO₂ (d), the error bar represents 100
 276 times randomly CV results.

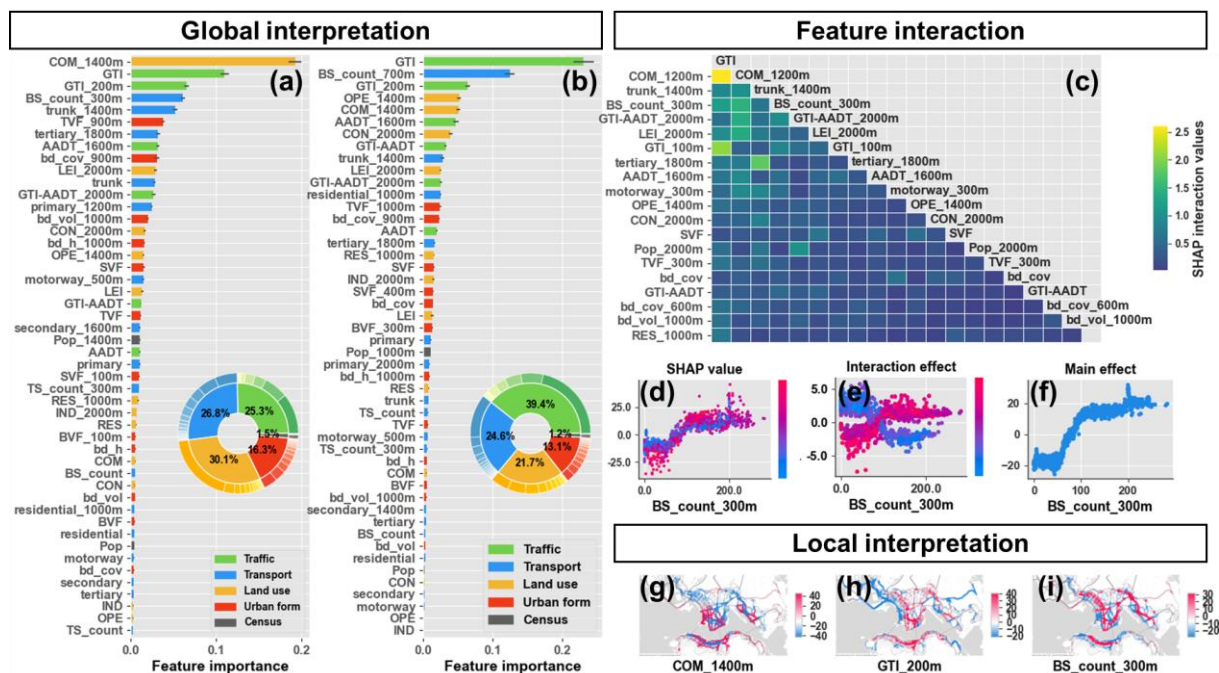
277
 278 The performance of four category models was compared in Figure 2(a,b), and the RMSE and
 279 MAPE results are detailed in Table S7. As a benchmark, the LUR model showed the lowest
 280 performance as expected with 5-fold CV R^2 of 0.41 and 0.36 for NO and NO₂, which indicates
 281 that the linear model can hardly explain the pollution variation in the complex urban
 282 environment (Lee et al., 2017; Miskell et al., 2015). The ML models present better performance
 283 than LUR model and vary with the mechanism. Generally, the classification tree-based models
 284 tend to show close performance and prediction results (Figure S12, S13), such as RF and XGB
 285 with delta R^2 within 0.02. For all base models, the CAT presents superior performance and was
 286 chosen as the final estimator for DF model. However, the stacking method (two layers stacking
 287 model) merely presents moderate performance instead of superior performance than base
 288 models as some studies found (Kerckhoffs et al., 2019; Liu et al., 2021; Shtein et al., 2019).
 289 When the stacking layer increased from 2 layers to 3 layers, the model performance even
 290 decreased at the cost of R^2 reduction of 0.04 for NO and 0.07 for NO₂ (Figure S14, Table S9)
 291 which indicates the complexity enhanced overfitting. For DL models, DNN presents mediocre
 292 performance with slight improvements compared with LUR model, while the CNN could
 293 extract hierarchical features in convolutional layers that improved performance compared to
 294 DNN. The DF model shows the highest performance with CV R^2 of 0.72 and 0.68 for NO and
 295 NO₂. Different from the stacking model, the DF model performance was constrained after layer-
 296 by-layer processing. The results suggest that, in addition to improving prediction performance,
 297 the DF model addressed both generalization and overfitting. To extensively assess the model
 298 generalization ability, we also evaluated route-based CV and spatial-block CV strategies. The
 299 route CV presents similar performance with random CV for all models. The model spatial
 300 extrapolation was expectedly undermined about 0.15-0.17 which is consistent with previous

301 studies (Lu et al., 2021). The comparison and DF model predictions could be seen in Figure
302 S15.

303 As a comparison of spatial variables construction schemes, we also evaluated segments-based
304 prediction and grid-based prediction using the DF model at the same spatial resolution (Figure
305 S16) which showed a strong consistency (*Pearson r* >0.85). On this basis, we investigated the
306 influence of spatial resolution on model performance using grid-based variables ranging from
307 50 m to 500 m ((Figure 2(c,d)). The fine-scale (50 m) grid-based model performance is close
308 to that of the segment-based model. Both NO and NO₂ model performance present decreasing
309 trend with the upscaling of resolution (Figure S17), suggesting that coarse resolution could
310 weaken the model prediction ability and result in a loss of spatial details. Correspondingly, NO
311 was more sensitive to spatial resolution than NO₂ indicating the hyperlocal variation effect
312 (Chambliss et al., 2021).

313 **3.2 Model Interpretation**

314 The global feature importance is presented in Figure 3(a,b). Transport infrastructure and traffic-
315 related features contribute the most, accounting for more than 52% and 64% for NO and NO₂.
316 Notably, our new traffic status variables rank top in feature importance, the on-road (GTI) and
317 neighborhood (within 200 m) traffic status can capture instant localized traffic activities and
318 are key contributors of traffic emissions. The introduction of GTI substantially improved model
319 prediction, increasing R^2 by 0.05-0.1 for non-linear models (Table S8). Concurrently, bus stop
320 density (BS_count), road length density and traffic volumes (AADT) influence pollutant
321 emission distributions. Unlike localized traffic status, commercial areas exert a wider influence
322 on pollution levels by directing transportation activities at a larger scale. Aside from emission
323 intensity related variables, urban form is another non-negligible factor that influences pollutant
324 dispersion or accumulation conditions (Shi et al., 2016). The shared top ranking features and
325 buffer radius suggest similarities in the driving factors and influence range for NO and NO₂
326 (Lee et al., 2017). Comparison of feature importance between base models (Figure S18, S19)
327 indicates that tree-based models exhibit similar feature rankings to the overall model
328 performance. Further, the SHAP summary plot provides evidence of variable influence
329 directions on model prediction for individual instances (Figure S20). Overall, traffic emission
330 related variables exhibit positive contributions, while variables related to dispersion status, e.g.,
331 the SVF that indicates openness of urban form, present negative effects.



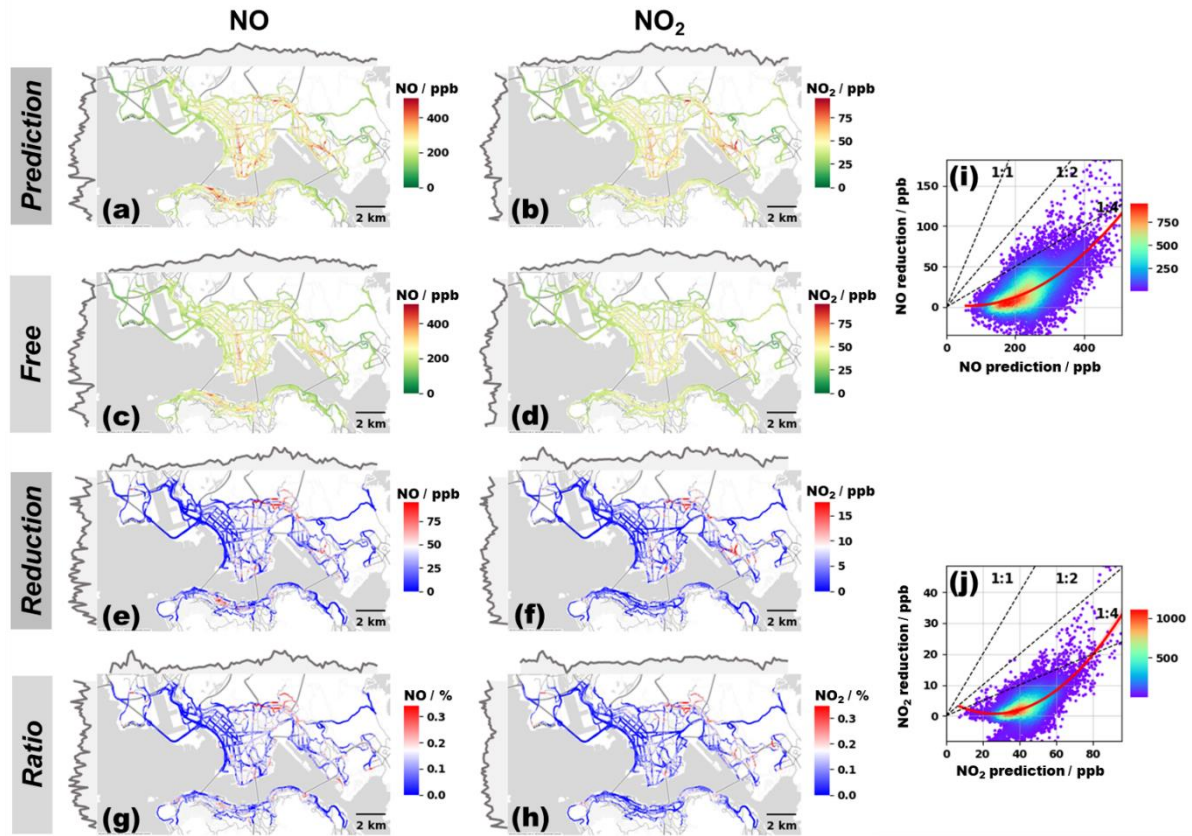
332
 333 Figure 3 SHAP explained global feature importance for NO (a) and NO₂ (b). The inset PieDonut contains
 334 categorized features (inner ring) and single variable contributions (out ring). The summary plots are presented in
 335 Figure S19. (c) The feature interaction values of the top 20 features for NO, the y-axis is interaction features which
 336 is ranked by mean interaction values. (d) SHAP values dependence plot for bus station count, the vertical
 337 dispersion dots indicate magnitude of interaction effects. The dots (measurements) are colored by traffic status and
 338 traffic volume (GTI-AADT), with red indicating congestion and high traffic values and blue indicating inverse.
 339 Vertical dispersions of colors depict the magnitude of interaction effect. (e) The separated interaction SHAP values
 340 between bus stop count and traffic status with volume. (f) The main effect SHAP values for bus stop density
 341 contribution to pollutant prediction. The spatial distribution of SHAP values for three top features for NO
 342 prediction: commercial land use (g), traffic status (h) and bus station distribution (i).

343
 344 Leveraged by SHAP dependence plot, we can better understand the relationships between
 345 pollutants and variations in each feature. Figure 3(d) illustrates the impact of bus stop density
 346 on the predictions of each measurement and presents positive contributions to pollutants with a
 347 nonlinear trend. Generally, most features exhibit non-monotonic trends suggesting that the
 348 influence of pollutants varies regionally (Figures S21-24, Text S7). This could explain the poor
 349 performance of the linear regression based LUR model in predicting pollutant variations.
 350 Except for univariate analysis, we investigated coupling intensities of main features with SHAP
 351 interaction values. Figure 3(c) presents feature interaction values for NO (Figure S25 for NO₂).
 352 To summarize, on-road pollution is driven by a combination of traffic status, transportation,
 353 land use and urban form. The ranking of feature interaction values closely aligns with individual
 354 feature importance, suggesting that on-road pollutions are not solely influenced by dominant
 355 features, but rather by feature interactions as well. The partial dependent plot in Figure 3(d)
 356 shows the combined effect contributions to SHAP values, the vertical dispersion of SHAP
 357 values for a certain of bus stop density (BS_count) value is due to the interaction effect with
 358 congestion and traffic volume (GTI_AADT). By decoupling the interaction effect from the
 359 feature contributions, we obtained main effect of BS_count in Figure 3(e) and feature

360 interaction SHAP values between BS_count with GTI_AADT in Figure 3(f). The main effect
361 illustrates positive contributions of bus stop density to SHAP values. The interaction presents a
362 positive contribution with the increase of BS_count and higher GTI_AADT (red dots), which
363 indicates high bus stop density (>100 for 300m buffer area) coupled with traffic congestion
364 enhanced pollution level collectively. An inverse case could be observed between urban form
365 factor (SVF) and traffic status in Figure S25. The negative interaction effect between increased
366 SVF values and high GTI indicates street openness could mitigate congestion induced pollution.
367 The turning point occurred at higher SVF values (>0.75). A summary of the interactions
368 between four types of key features is shown in Figure S26 and explained in Text S6.
369 The SHAP interpretation map emphasizes the importance of local (each road segment)
370 contributions and indicates regions where variables have positive or negative associations with
371 the TRAP. We estimated the contributions of the three most important features SHAP values
372 for NO in Figure 3(g,h,i). High-density commercial area (COM_1400m) is mainly along the
373 periphery of Hong Kong Island and the tip area of the Kowloon Peninsula, resulting in the
374 highest positive SHAP values. The traffic status (GTI_200m) emphasizes that congestion-
375 related contributions are concentrated along certain roads. The SHAP value for bus stop exhibits
376 an aggregated spatial pattern that indicates the potential for TRAP accumulation. Conversely, a
377 lower station density design could help mitigate TRAP with negative SHAP values. Figure S27,
378 S28 and Text S6 give the summary of main feature SHAP maps for NO and NO₂. From a
379 comprehensive perspective, the sum of individual SHAP values forms the final prediction, with
380 pollution variation explained by discrepancies in feature compositions.

381 **3.3 Predictions and Traffic Congestion Impacts**

382 The on-road TRAP estimations are illustrated in Figure 4(a,b). Dissimilar to the highway-
383 dominated elevated pattern (Apte et al., 2017; J. Miller et al., 2020), NO and NO₂
384 concentrations in Hong Kong exhibit centralized spatial patterns (projected profiles), with
385 major road hotspots mainly identified in core urban areas (Che et al., 2023; Lee et al., 2017).
386 Generally, heavy pollution is distributed at Central, Causeway Bay areas which are Hong Kong
387 AQMS monitoring areas, as well as in Kwun Tong area and Hung Hom Tunnel entrance where
388 there is heavy traffic activity. High concentrations are also observed along Nathan Road, which
389 is surrounded by high-density buildings. Grid-based predictions also present similar
390 distributions (Figure S17).



391
 392 Figure 4 The prediction of on-road concentrations of current status (a, b) and free status (c, d) for NO and NO₂ in
 393 the study area. The estimated reductions (e,f) are due to the improved traffic status and the ratio of the reduction
 394 compared to base prediction (g,h). The correlations between reduction and base prediction that marked with point
 395 density (i,j). Dash lines represent 1:4 (25% reduction), 1:2 (50% reduction) and 1:1 (100% reduction) relationship.
 396 The red lines are quadratic fit curves of reduction corresponding to predicted pollution.

397 The predictions of congestion-free status are shown in Figure 4(c,d). The pollution abatement
 398 was calculated based on the predictive comparative analysis in Figure 4(e,f). The reductions
 399 presented a heterogenous and aggregating pattern as pollution distributions. Globally, pollution
 400 reductions in most of road segments are limited (below 10%) that can hardly benefit from the
 401 eliminated congestion. Whereas individual road segments could benefit from higher reductions
 402 with more than 25% or even as high as 50% (Figure 4(i,j)). Interestingly, the reduction hotspots
 403 coincide with pollution hotspot areas and enhanced reductions with the increase in pollution
 404 levels (Figure 4(g,h)). In other words, the congestion induced pollution plays a key role in
 405 heavily polluted road segments, and the elimination of heavily congested areas could gain
 406 augmented benefits (Table S10). The spatial co-occurrence of congestion-induced air pollutants
 407 indicates analogous emission patterns for NO and NO₂. Additionally, they also exhibit diurnal
 408 variation markedly, with peak levels observed during rush hours, and display consistent spatial
 409 patterns (Figure S29, S30). Similar rates of reduction were observed in the causal analysis and
 410 consistent with the predictive analysis (Table S10, Figure S31). On average, the reductions
 411 estimated from predictive comparative analysis are 7.7% and 5.1% for NO and NO₂, while 6.6%
 412 and 6.7% from causal analysis. Nevertheless, some variations in spatial distribution could be
 413 observed (Figure S32). This suggests that while there is a correlation between traffic status and

414 pollution levels, the causal analysis also plays a more nuanced role, within which specific traffic
415 conditions may exert a direct influence on the degree and distribution of TRAPs.

416 **4 DISCUSSION**

417 **4.1 Street-Level Air Quality Model Development, Interpretation and Predictions**

418 The base LUR model displayed the lowest performance and was poor than other cities (Table
419 S11), indicating that the linear relationship constrains the description of pollutant variation,
420 particularly in Hong Kong's intricate urban setting (Lee et al., 2017; Miskell et al., 2015; Ren
421 et al., 2020). Lee et al. (Lee et al., 2017) reported lower LUR model performances for roadside
422 sampling in Hong Kong, with CV R^2 0.28 and 0.39 for NO and NO₂. The ML model
423 performance improved significantly through non-linear regressions. As a comparison, our base
424 model prediction presents worthy performance among existing models (Table S11).
425 Nevertheless, the main target of this study is not simply comparing with previous works or
426 intercomparison of existing models, since ML models performance is context-based and may
427 vary with urban environments and measurements (Kerckhoffs et al., 2019). Instead, improving
428 existing model performance is prioritized in this work. Given that the model complexity is an
429 indispensable condition for improving model performance (Poggio et al., 2020; Reichstein et
430 al., 2019), we constructed the model in two dimensions: 1) model diversity by integrating
431 various models; and 2) model structure by increasing the model depth. The stacking model
432 followed this path and exhibited good performance in a number of studies (Lim et al., 2019;
433 Liu et al., 2021; Shtein et al., 2019). However, it merely reached a moderate performance
434 among base models and decreased with layers indicates overfitting constrained model
435 performance. In other words, the stacking model induction ability was enhanced with depth,
436 while the measurement noises or specificities were also learned in the training process,
437 undermining model generalization ability. Our reconstructed DF model performed superior to
438 other models by integrating diversiform models with a flexible structure, which adjusts
439 complexity (layer number) adaptively instead of hyper-parameter tuning (Zhou and Feng, 2019).
440 Furthermore, the DF model reached stable performance after layer-by-layer processing rather
441 than relying on backpropagation or gradient descent for generalization in NN-structured DL
442 models which are sensitive to model structure and hyperparameters.

443 The model resolution represents its ability to capture pollution hotspots and fine-scale spatial
444 variations, which are crucial for accurately estimating personal exposure in environmental
445 justice studies (Gardner-Frolick et al., 2022). The decreasing trend in model performance
446 associated with upscaled measurements and variables implies that the prediction capacity to
447 capture hyperlocal pollution variations at fine scales diminishes. This can be attributed to two
448 main factors: 1) street-level TRAP measurements display localized variations but are detrended
449 at coarser-scale backgrounds; 2) fine-scale variables like GTI better reflect localized pollution
450 variations from direct emissions (Tang et al., 2013), which weakens at coarser scales. Our
451 findings underscore the need for both fine-scale mobile campaigns and variables in street-level
452 air quality model construction, as the former captures hyperlocal TRAP variations and the latter

453 provides information directly related to street-level traffic emissions.
454 Besides enhancing prediction performance, comprehending feature-driven complexity and
455 interactions is vital for demystifying ML models' "black box" nature. Globally, transport
456 infrastructure and traffic-related variables contribute most to TRAP at street-level environments
457 (Hatzopoulou et al., 2017; Lee et al., 2017; Miskell et al., 2015). The newly introduced GTI
458 ranks the top predictor and presents substantial improvements in TRAP estimations. It could
459 capture fine-scale traffic pattern variations related to localized vehicle fleet activities (Figure
460 S33), while buffered GTI variables emphasize the neighborhood impact of congestion-induced
461 traffic emissions. Crowdsourced traffic data offers near real-time information compared to
462 traditional geographic variables, enabling rapid response to urban infrastructure construction.
463 Combining open access data enables more mobile campaign deployment opportunities in
464 multiple cities, facilitating intercity model building and street-level traffic pollution estimation
465 in information-limited areas (Zalzal et al., 2019). Furthermore, real-time traffic data can provide
466 localized road statuses like blockages or accidents that directly impact traffic emissions and
467 serve as a crucial driver for spatiotemporal air quality model building and prediction. Other
468 traffic-related variables, confirmed in prior studies (Jain et al., 2021; Lee et al., 2017), include
469 road length as a crucial model prediction feature, while dominant road types may differ with
470 surroundings. Bus stop density also serves as a significant estimator. Given public transport's
471 vital role in Hong Kong, bus station arrangements can affect pollutant emissions in central urban
472 or CBD areas locally (Ma et al., 2019; Miskell et al., 2015; Weissert et al., 2018). The
473 introduction of VFs contributes to explain pollutant dispersion, especially in street-level scenes,
474 and serves as attainable factors for keeping up with mobile measurements. Specifically, the SVF
475 exhibits a negative effect, signifying the influence on pollutant dispersion status.
476 Feature interaction is rarely examined in urban air quality models that can intensify or mitigate
477 pollution (Kerckhoffs et al., 2019), highlighting synergistic rather than univariate influences.
478 These feature interactions varied with informative characteristics for implementing effective
479 pollution control strategies. The neglect of features interplay effect may partially account
480 for the linear regression model's lower performance (Miskell et al., 2015). The feature localized
481 interpretation was implemented to understand the extent of feature contribution, indicating
482 regions where features had positive or negative contributions to on-road pollution, enabling
483 refined street-level pollution control management. The interpretation allows for the
484 identification of significant feature contributions specific to each road segment and aids in
485 prioritizing management efforts accordingly, which allows to comprehensively understand
486 variability in pollutant concentrations and design effective guidelines for urban plannings
487 (Huang et al., 2021).
488 Our prediction identified localized TRAP hotspots were mainly located in high-rise buildings
489 and congested commercial areas, which aligned with LUR model and the latest fine-scale
490 dispersion model in Hong Kong (Che et al., 2023; Lee et al., 2017). In contrast to previous
491 studies focused on global traffic emission estimations to assess pollution control effects
492 (Matthias et al., 2020), we designed two strategies to assess the impact of improvements in
493 human-intervened traffic transition scenario on reducing TRAP.
494 At the macro scale, the eliminated congestion yielded limited reductions (5%-8%). This is
495 because heavy congestion only takes place in 6% of road segments (and 3% experienced

496 constant congestion) while 80% keep good traffic flow (Figure S34). Correspondingly, the
497 causal analysis supplemented prediction results and confirming the effectiveness of human
498 interventions in reducing TRAP. While alleviating traffic congestion may only lead to a limited
499 reduction in pollution, its significance lies in maximizing environmental benefits for localized
500 air quality, particularly during peak hours. Overall, our analysis suggests that increasing the
501 usage of low-emission vehicles and tightening emission standards are essential for achieving
502 broad emission reductions (Wang et al., 2020). However, addressing traffic congestion
503 concurrently can yield greater environmental benefits in areas with high population density.

504 **4.2 Limitations and Future Works**

505 To comprehend the applicability of this study and direct future research, several limitations
506 should be taken into account. Firstly, while the bus platform campaign with repeated routes
507 ensured sample site visitation, it limited the spatial coverage of urban pollution. The sample
508 size is a critical issue, as validating model universality and performance necessitates large-scale
509 datasets, especially in cities with high road density. Reduced model performance in spatial CV
510 indicates that imbalanced spatial distribution of pollutants may hinder the model's spatial
511 prediction capabilities with limited sampling segments. Google View cars have exhibited a
512 random drive-by paradigm that facilitates extensive spatial coverage (Apte et al., 2017). Mobile
513 sensing capabilities can be improved by randomly dispatching vehicle fleets, simultaneously
514 expanding coverage in both spatial and temporal dimensions (O’Keeffe et al., 2019). Secondly,
515 defining the traffic index as a proxy for real traffic intensity status rather than traffic speed may
516 weaken traffic status representation in different road contexts. Considering that bus speed is
517 generally lower than vehicle fleet speed, incorporating large-scale taxi fleets could provide a
518 more reliable road speed measurement and support fine-scale emission inventory estimation in
519 future research. Thirdly, it should be clarified that our model and campaign aim to estimate on-
520 road pollutant variations rather than area surface predictions, even though we have achieved
521 grid-based surface predictions with comparable performance. We assume that a comprehensive
522 urban profile can be best explained through the integration of mobile-based and fixed-site-based
523 models. The two components represent distinct urban pollution patterns with inherently
524 inconsistent driving factors. The on-road pollutants presented highly localized variation that
525 mainly driven by local features, while urban background pollution is driven by localized
526 features and regional influence in combination. As air sensor applications in fixed and mobile
527 networks increase, developing models that fuse these two paradigms could become a significant
528 area of future research. Finally, it should be noted that our scenario analysis for TRAP
529 prediction reduction could be further refined. While the predictive comparative analysis is
530 effective in identifying patterns, it relies on correlation rather than causality, which could also
531 influence 'what-if' pollution levels. Similarly, the causal analysis makes specific assumptions
532 about certain confounding features, which may not fully capture the complexity of real-world
533 traffic and pollution dynamics. To enhance the applicability and robustness of our model, it is
534 crucial to assess model performance across a variety of urban environments and to incorporate
535 environmental changes that may impact air pollution dynamics. This includes considering
536 factors such as meteorological variations, land use patterns, and the influence of secondary

537 pollutants. thereby providing a more comprehensive and adaptable framework for urban air
538 pollution modeling. Therefore, despite our work offering potential pathways for improving air
539 quality estimations and predicting the impact of targeted policy interventions, further research
540 is required to fully understand the multifaceted relationship between traffic congestion and air
541 pollution.
542

543 **5 Conclusion**

544 In this study, we built a thorough framework for prediction, analysis, and evaluation with human
545 interventions. A deep learning-based air model was developed to predict fine-scale TRAP
546 spatial distribution, achieving R^2 values of 0.72 for NO and 0.69 for NO₂, demonstrating
547 excellent performance in complex urban environments. Incorporating real-time Google traffic
548 data—a new, effective, and accessible data source—markedly improved model accuracy,
549 underscoring the importance of traffic patterns in estimating TRAP. The interpretable machine
550 learning method revealed the significance of traffic-related features and key contributions of
551 the newly introduced traffic index that facilitated rapid responses to urban infrastructure
552 changes. Recognizing feature interactions highlighted their synergistic effects on pollution,
553 leading to more nuanced and effective pollution control strategies. Meanwhile, the localized
554 interpretation aids in identifying regions where feature contributions vary, allowing for refined
555 street-level pollution management and the design of effective urban planning guidelines. The
556 scenario provides detailed insights into TRAP abatement, highlighting that while alleviating
557 traffic congestion yields limited reductions in pollution, it maximizes environmental benefits
558 for localized air quality during peak hours. The integration of a high-performance model and
559 new data improves prediction accuracy and deepens our understanding of the variables affecting
560 air quality, which is essential for informing future policy and environmental initiatives.

561 **ACKNOWLEDGEMENT**

562 This study was supported by General Research Fund (GRF) of Hong Kong Special
563 Administrative Region, China (16212022, 2022-2023), Environment and Conservation Fund
564 (ECF/21/2021).
565

566 **REFERENCES**

- 567 Apte, J.S., Messier, K.P., Gani, S., Brauer, M., Kirchstetter, T.W., Lunden, M.M., Marshall, J.D., Portier, C.J.,
568 Vermeulen, R.C.H., Hamburg, S.P., 2017. High-Resolution Air Pollution Mapping with Google Street View
569 Cars: Exploiting Big Data. *Environ. Sci. Technol.* 51, 6999–7008. <https://doi.org/10.1021/acs.est.7b00891>
- 570 Baron, R., Saffell, J., 2017. Amperometric Gas Sensors as a Low Cost Emerging Technology Platform for Air

571 Quality Monitoring Applications: A Review. ACS Sensors 2, 1553–1566.
572 <https://doi.org/10.1021/ACSSENSORS.7B00620>

573 Briggs, D., 2006. The Role of Gis: Coping With Space (And Time) in Air Pollution Exposure Assessment.
574 <http://dx.doi.org/10.1080/15287390590936094> 68, 1243–1261.
575 <https://doi.org/10.1080/15287390590936094>

576 C. Simon, M., P. Patton, A., N. Naumova, E., I. Levy, J., Kumar, P., Brugge, D., L. Durant, J., 2018. Combining
577 Measurements from Mobile Monitoring and a Reference Site To Develop Models of Ambient Ultrafine
578 Particle Number Concentration at Residences. Environ. Sci. & Technol. 52, 6985–6995.
579 <https://doi.org/10.1021/acs.est.8b00292>

580 Chambliss, S.E., Pinon, C.P.R., Messier, K.P., LaFranchi, B., Upperman, C.R., Lunden, M.M., Robinson, A.L.,
581 Marshall, J.D., Apte, J.S., 2021. Local- And regional-scale racial and ethnic disparities in air pollution
582 determined by long-term mobile monitoring. Proc. Natl. Acad. Sci. U. S. A. 118.
583 <https://doi.org/10.1073/pnas.2109249118>

584 Che, W., Zhang, Y., Lin, C., Fung, Y.H., Fung, J.C.H., Lau, A.K.H., 2023. Impacts of pollution heterogeneity on
585 population exposure in dense urban areas using ultra-fine resolution air quality data. J. Environ. Sci. 125,
586 513–523. <https://doi.org/10.1016/J.JES.2022.02.041>

587 Chen, D., Hu, F., Nian, G., Yang, T., 2020. Deep Residual Learning for Nonlinear Regression. Entropy 2020, Vol.
588 22, Page 193 22, 193. <https://doi.org/10.3390/E22020193>

589 Chen, H., Kwong, J.C., Copes, R., Tu, K., Villeneuve, P.J., van Donkelaar, A., Hystad, P., Martin, R. V., Murray,
590 B.J., Jessiman, B., Wilton, A.S., Kopp, A., Burnett, R.T., 2017. Living near major roads and the incidence
591 of dementia, Parkinson’s disease, and multiple sclerosis: a population-based cohort study. Lancet 389, 718–
592 726. [https://doi.org/10.1016/S0140-6736\(16\)32399-6](https://doi.org/10.1016/S0140-6736(16)32399-6)

593 Dalgleish, T., Williams, J.M.G., Golden, A.-M.J., Perkins, N., Barrett, L.F., Barnard, P.J., Au Yeung, C., Murphy,
594 V., Elward, R., Tchaturia, K., Watkins, E., 2018. Mapping Air Pollution with Google Street View Cars:
595 Efficient Approaches with Mobile Monitoring and Land Use Regression(SI). J. Exp. Psychol. Gen. 136, 23–
596 42.

597 Delfino, R.J., Staimer, N., Tjoa, T., Gillen, D., Kleinman, M.T., Sioutas, C., Cooper, D., 2008. Personal and
598 ambient air pollution exposures and lung function decrements in children with asthma. Environ. Health
599 Perspect. 116, 550–558. <https://doi.org/10.1289/ehp.10911>

600 Deville Cavellin, L., Weichenthal, S., Tack, R., S. Ragettli, M., Smargiassi, A., Hatzopoulou, M., 2015.
601 Investigating the Use Of Portable Air Pollution Sensors to Capture the Spatial Variability Of Traffic-Related
602 Air Pollution. Environ. Sci. & Technol. 50, 313–320. <https://doi.org/10.1021/acs.est.5b04235>

603 Di, Q., Amini, H., Shi, L., Kloog, I., Silvern, R., Kelly, J., Sabath, M.B., Choirat, C., Koutrakis, P., Lyapustin, A.,
604 Wang, Y., Mickley, L.J., Schwartz, J., 2019. Assessing NO2 Concentration and Model Uncertainty with
605 High Spatiotemporal Resolution across the Contiguous United States Using Ensemble Model Averaging.

606 Environ. Sci. Technol. 54, 1372–1384. <https://doi.org/10.1021/ACS.EST.9B03358>

607 Di, Q., Kloog, I., Koutrakis, P., Lyapustin, A., Wang, Y., Schwartz, J., 2016. Assessing PM_{2.5} Exposures with
608 High Spatiotemporal Resolution across the Continental United States. *Environ. Sci. Technol.* 50, 4712–4721.
609 <https://doi.org/10.1021/ACS.EST.5B06121>

610 Ding, Y., Chen, Z., Lu, W., Wang, X., 2021. A CatBoost approach with wavelet decomposition to improve
611 satellite-derived high-resolution PM_{2.5} estimates in Beijing-Tianjin-Hebei. *Atmos. Environ.* 249, 118212.
612 <https://doi.org/10.1016/J.ATMOSENV.2021.118212>

613 Emporis, 2018. Hong Kong building types [WWW Document]. URL
614 <https://www.emporis.com/city/101300/hong-kong-china>

615 Gardner-Frolick, R., Boyd, D., Giang, A., 2022. Selecting Data Analytic and Modeling Methods to Support Air
616 Pollution and Environmental Justice Investigations: A Critical Review and Guidance Framework. *Environ.*
617 *Sci. Technol.* <https://doi.org/10.1021/acs.est.1c01739>

618 Gately, C.K., Hutyra, L.R., Peterson, S., Sue Wing, I., 2017. Urban emissions hotspots: Quantifying vehicle
619 congestion and air pollution using mobile phone GPS data. *Environ. Pollut.* 229, 496–504.
620 <https://doi.org/10.1016/J.ENVPOL.2017.05.091>

621 Gerges, F., Llaguno-Munitxa, M., Zondlo, M.A., Boufadel, M.C., Bou-Zeid, E., 2024. Weather and the City:
622 Machine Learning for Predicting and Attributing Fine Scale Air Quality to Meteorological and Urban
623 Determinants. *Environ. Sci. Technol.* 58. <https://doi.org/10.1021/acs.est.4c00783>

624 Gong, F.-Y., Zeng, Z.-C., Zhang, F., Li, X., Ng, E., Norford, L.K., 2018. Mapping sky, tree, and building view
625 factors of street canyons in a high-density urban environment. *Build. Environ.* 134, 155–167.
626 <https://doi.org/10.1016/J.BUILDENV.2018.02.042>

627 Google Maps, 2009. Official Google Blog: The bright side of sitting in traffic: Crowdsourcing road congestion
628 data [WWW Document]. URL [https://googleblog.blogspot.com/2009/08/bright-side-of-sitting-in-](https://googleblog.blogspot.com/2009/08/bright-side-of-sitting-in-traffic.html)
629 [traffic.html](https://googleblog.blogspot.com/2009/08/bright-side-of-sitting-in-traffic.html) (accessed 6.23.21).

630 Grange, S.K., Lewis, A.C., Moller, S.J., Carslaw, D.C., 2017. Lower vehicular primary emissions of NO₂ in
631 Europe than assumed in policy projections. *Nat. Geosci.* 10, 914–918. [https://doi.org/10.1038/s41561-017-](https://doi.org/10.1038/s41561-017-0009-0)
632 [0009-0](https://doi.org/10.1038/s41561-017-0009-0)

633 Guarnieri, M., Balmes, J.R., 2014. Outdoor air pollution and asthma. *Lancet.* [https://doi.org/10.1016/S0140-](https://doi.org/10.1016/S0140-6736(14)60617-6)
634 [6736\(14\)60617-6](https://doi.org/10.1016/S0140-6736(14)60617-6)

635 Hancock, J.T., Khoshgoftaar, T.M., 2020. CatBoost for big data: an interdisciplinary review. *J. Big Data* 7, 1–45.
636 <https://doi.org/10.1186/S40537-020-00369-8/FIGURES/9>

637 Hankey, S., D. Marshall, J., 2015. Land Use Regression Models of On-Road Particulate Air Pollution (Particle
638 Number, Black Carbon, PM_{2.5}, Particle Size) Using Mobile Monitoring. *Environ. Sci. & Technol.* 49,

- 639 9194–9202. <https://doi.org/10.1021/acs.est.5b01209>
- 640 Hankey, S., Lindsey, G., Marshall, J.D., 2017. Population-Level Exposure to Particulate Air Pollution during
641 Active Travel: Planning for Low-Exposure, Health-Promoting Cities. *Environ. Health Perspect.* 125, 527–
642 534. <https://doi.org/10.1289/EHP442>
- 643 Hankey, S., Sforza, P., Pierson, M., 2019. Using Mobile Monitoring to Develop Hourly Empirical Models of
644 Particulate Air Pollution in a Rural Appalachian Community. *Environ. Sci. & Technol.* 53, 4305–4315.
645 <https://doi.org/10.1021/acs.est.8b05249>
- 646 Harrison, R.M., Vu, T. Van, Jafar, H., Shi, Z., 2021. More mileage in reducing urban air pollution from road traffic.
647 *Environ. Int.* 149, 106329. <https://doi.org/10.1016/j.envint.2020.106329>
- 648 Hatzopoulou, M., France Valois, M., Levy, I., Mihele, C., Lu, G., Bagg, S., Minet, L., Brook, J., 2017. Robustness
649 of Land-Use Regression Models Developed from Mobile Air Pollutant Measurements. *Environ. Sci. &
650 Technol.* 51, 3938–3947. <https://doi.org/10.1021/acs.est.7b00366>
- 651 Hatzopoulou, M., Weichenthal, S., Dugum, H., Pickett, G., Miranda-Moreno, L., Kulka, R., Andersen, R.,
652 Goldberg, M., 2012. The impact of traffic volume, composition, and road geometry on personal air pollution
653 exposures among cyclists in Montreal, Canada. *J. Expo. Sci. Environ. Epidemiol.* 2013 231 23, 46–51.
654 <https://doi.org/10.1038/jes.2012.85>
- 655 HEI, 2010. Traffic-Related Air Pollution: A Critical Review of the Literature on Emissions, Exposure, and Health
656 Effects. Spec. Rep.
- 657 Hilpert, M., Johnson, M., Kioumourtzoglou, M.-A., Domingo-Relloso, A., Peters, A., Adria-Mora, B., Hernández,
658 D., Ross, J., Chillrud, S.N., 2019. A new approach for inferring traffic-related air pollution: Use of radar-
659 calibrated crowd-sourced traffic data. *Environ. Int.* 127, 142–159.
660 <https://doi.org/10.1016/J.ENVINT.2019.03.026>
- 661 Hoek, G., Beelen, R., de Hoogh, K., Vienneau, D., Gulliver, J., Fischer, P., Briggs, D., 2008a. A review of land-
662 use regression models to assess spatial variation of outdoor air pollution. *Atmos. Environ.* 42, 7561–7578.
663 <https://doi.org/10.1016/J.ATMOSENV.2008.05.057>
- 664 Hoek, G., Beelen, R., de Hoogh, K., Vienneau, D., Gulliver, J., Fischer, P., Briggs, D., 2008b. A review of land-
665 use regression models to assess spatial variation of outdoor air pollution. *Atmos. Environ.* 42, 7561–7578.
666 <https://doi.org/10.1016/J.ATMOSENV.2008.05.057>
- 667 Hoek, G., Brunekreef, B., Goldbohm, S., Fischer, P., Van Den Brandt, P.A., 2002. Association between mortality
668 and indicators of traffic-related air pollution in the Netherlands: a cohort study. *Lancet* 360, 1203–1209.
669 [https://doi.org/10.1016/S0140-6736\(02\)11280-3](https://doi.org/10.1016/S0140-6736(02)11280-3)
- 670 Hu, C.B., Zhang, F., Gong, F.Y., Ratti, C., Li, X., 2020. Classification and mapping of urban canyon geometry
671 using Google Street View images and deep multitask learning. *Build. Environ.* 167, 106424.
672 <https://doi.org/10.1016/j.buildenv.2019.106424>

673 Hu, X., Belle, J.H., Meng, X., Wildani, A., Waller, L.A., Strickland, M.J., Liu, Y., 2017. Estimating PM2.5
674 Concentrations in the Conterminous United States Using the Random Forest Approach. *Environ. Sci.*
675 *Technol.* 51, 6936–6944. <https://doi.org/10.1021/ACS.EST.7B01210>

676 Huang, Y., Lei, C., Liu, C.-H., Perez, P., Forehead, H., Kong, S., Zhou, J.L., 2021. A review of strategies for
677 mitigating roadside air pollution in urban street canyons. *Environ. Pollut.* 280, 116971.
678 <https://doi.org/10.1016/j.envpol.2021.116971>

679 J. Miller, D., Actkinson, B., Padilla, L., J. Griffin, R., Moore, K., Grace Tee Lewis, P., Gardner-Frolick, R., Craft,
680 E., J. Portier, C., P. Hamburg, S., A. Alvarez, R., 2020. Characterizing Elevated Urban Air Pollutant Spatial
681 Patterns with Mobile Monitoring in Houston, Texas. *Environ. Sci. & Technol.* 0.
682 <https://doi.org/10.1021/acs.est.9b05523>

683 Jain, S., Presto, A.A., Zimmerman, N., 2021. Spatial Modeling of Daily PM2.5, NO2, and CO Concentrations
684 Measured by a Low-Cost Sensor Network: Comparison of Linear, Machine Learning, and Hybrid Land Use
685 Models. *Environ. Sci. Technol.* 55, 8641. <https://doi.org/10.1021/ACS.EST.1C02653>

686 Ji, N., Baptista, A., Yu, C.H., Cepeda, C., Green, F., Greenberg, M., Mincey, I.C., Ohman-Strickland, P., Fiedler,
687 N., Kipen, H.M., Laumbach, R.J., 2024. Traffic-related air pollution, chronic stress, and changes in exhaled
688 nitric oxide and lung function among a panel of children with asthma living in an underresourced community.
689 *Sci. Total Environ.* 912. <https://doi.org/10.1016/j.scitotenv.2023.168984>

690 Kerckhoffs, J., Hoek, G., Portengen, L., Brunekreef, B., Vermeulen, R.C.H., 2019. Performance of Prediction
691 Algorithms for Modeling Outdoor Air Pollution Spatial Surfaces. *Environ. Sci. Technol.* 53.
692 <https://doi.org/10.1021/acs.est.8b06038>

693 Kim, J.J., Smorodinsky, S., Lipsett, M., Singer, B.C., Hodgson, A.T., Ostro, B., 2004. Traffic-related Air Pollution
694 near Busy Roads. *Am. J. Respir. Crit. Care Med.* 170, 520–526. <https://doi.org/10.1164/rccm.200403-281OC>

696 Kumar, P., Morawska, L., Martani, C., Biskos, G., Neophytou, M., Di Sabatino, S., Bell, M., Norford, L., Britter,
697 R., 2015. The rise of low-cost sensing for managing air pollution in cities. *Environ. Int.*
698 <https://doi.org/10.1016/j.envint.2014.11.019>

699 Lee, M., Brauer, M., Wong, P., Tang, R., Tsui, T.H., Choi, C., Cheng, W., Lai, P.-C., Tian, L., Thach, T.-Q., Allen,
700 R., Barratt, B., 2017. Land use regression modelling of air pollution in high density high rise cities: A case
701 study in Hong Kong. *Sci. Total Environ.* 592, 306–315. <https://doi.org/10.1016/J.SCITOTENV.2017.03.094>

702 Li, T., Shen, H., Yuan, Q., Zhang, X., Zhang, L., 2017. Estimating Ground-Level PM2.5 by Fusing Satellite and
703 Station Observations: A Geo-Intelligent Deep Learning Approach. *Geophys. Res. Lett.* 44, 11,985-11,993.
704 <https://doi.org/10.1002/2017GL075710>

705 Li, X., Ratti, C., 2019. Mapping the spatio-temporal distribution of solar radiation within street canyons of Boston
706 using Google Street View panoramas and building height model. *Landsc. Urban Plan.* 191, 103387.
707 <https://doi.org/10.1016/j.landurbplan.2018.07.011>

- 708 Li, X., Ratti, C., Seiferling, I., 2018. Quantifying the shade provision of street trees in urban landscape: A case
709 study in Boston, USA, using Google Street View. *Landsc. Urban Plan.* 169, 81–91.
710 <https://doi.org/10.1016/j.landurbplan.2017.08.011>
- 711 Li, Y., Tan, Z., Ye, C., Wang, J., Wang, Yanwen, Zhu, Y., Liang, P., Chen, X., Fang, Y., Han, Y., Wang, Q., He,
712 D., Wang, Yao, Zhu, T., 2019. Using wavelet transform to analyse on-road mobile measurements of air
713 pollutants: a case study to evaluate vehicle emission control policies during the 2014 APEC summit. *Atmos.*
714 *Chem. Phys.* 19, 13841–13857. <https://doi.org/10.5194/acp-19-13841-2019>
- 715 Lim, C.C., Kim, H., Vilcassim, M.J.R., Thurston, G.D., Gordon, T., Chen, L.-C., Lee, K., Heimbinder, M., Kim,
716 S.-Y., 2019. Mapping urban air quality using mobile sampling with low-cost sensors and machine learning
717 in Seoul, South Korea. *Environ. Int.* 131, 105022. <https://doi.org/10.1016/J.ENVINT.2019.105022>
- 718 Liu, X., Taylor, M.P., Aelion, C.M., Dong, C., 2021. Novel Application of Machine Learning Algorithms and
719 Model-Agnostic Methods to Identify Factors Influencing Childhood Blood Lead Levels. *Environ. Sci.*
720 *Technol.* 55, 13387–13399.
721 https://doi.org/10.1021/ACS.EST.1C01097/ASSET/IMAGES/LARGE/ES1C01097_0007.JPEG
- 722 Lloyd, M., Ganji, A., Xu, J., Venuta, A., Simon, L., Zhang, M., Saeedi, M., Yamanouchi, S., Apte, J., Hong, K.,
723 Hatzopoulou, M., Weichenthal, S., 2023. Predicting spatial variations in annual average outdoor ultrafine
724 particle concentrations in Montreal and Toronto, Canada: Integrating land use regression and deep learning
725 models. *Environ. Int.* 178. <https://doi.org/10.1016/j.envint.2023.108106>
- 726 Lu, T., Marshall, J.D., Zhang, W., Hystad, P., Kim, S.Y., Bechle, M.J., Demuzere, M., Hankey, S., 2021. National
727 Empirical Models of Air Pollution Using Microscale Measures of the Urban Environment. *Environ. Sci.*
728 *Technol.* 55, 15519–15530.
729 https://doi.org/10.1021/ACS.EST.1C04047/ASSET/IMAGES/LARGE/ES1C04047_0003.JPEG
- 730 Lundberg, S., Lee, S.-I., 2017. A Unified Approach to Interpreting Model Predictions.
- 731 Lyu, B., Hu, Y., Zhang, W., Du, Y., Luo, B., Sun, X., Sun, Z., Deng, Z., Wang, Xiaojiang, Liu, J., Wang, Xuesong,
732 Russell, A.G., 2019. Fusion Method Combining Ground-Level Observations with Chemical Transport
733 Model Predictions Using an Ensemble Deep Learning Framework: Application in China to Estimate
734 Spatiotemporally-Resolved PM_{2.5} Exposure Fields in 2014–2017. *Environ. Sci. Technol.* 53, 7306–7315.
735 https://doi.org/10.1021/ACS.EST.9B01117/SUPPL_FILE/ES9B01117_SI_001.PDF
- 736 Ma, X., Longley, I., Gao, J., Kachhara, A., Salmond, J., 2019. A site-optimised multi-scale GIS based land use
737 regression model for simulating local scale patterns in air pollution. *Sci. Total Environ.* 685, 134–149.
738 <https://doi.org/10.1016/j.scitotenv.2019.05.408>
- 739 Matthias, V., Bieser, J., Mocanu, T., Pregger, T., Quante, M., Ramacher, M.O.P., Seum, S., Winkler, C., 2020.
740 Modelling road transport emissions in Germany – Current day situation and scenarios for 2040. *Transp. Res.*
741 *Part D Transp. Environ.* 87, 102536. <https://doi.org/10.1016/J.TRD.2020.102536>
- 742 Mead, M.I., Popoola, O.A.M., Stewart, G.B., Landshoff, P., Calleja, M., Hayes, M., Baldovi, J.J., McLeod, M.W.,

- 743 Hodgson, T.F., Dicks, J., Lewis, A., Cohen, J., Baron, R., Saffell, J.R., Jones, R.L., 2013. The use of
744 electrochemical sensors for monitoring urban air quality in low-cost, high-density networks. *Atmos. Environ.*
745 <https://doi.org/10.1016/j.atmosenv.2012.11.060>
- 746 Miskell, G., Salmond, J., Longley, I., N. Dirks, K., 2015. A Novel Approach in Quantifying the Effect of Urban
747 Design Features on Local-Scale Air Pollution in Central Urban Areas. *Environ. Sci. & Technol.* 49,
748 9004–9011. <https://doi.org/10.1021/acs.est.5b00476>
- 749 Molnar, C., 2019. *Interpretable Machine Learning. A Guide for Making Black Box Models Explainable.* Book
750 247.
- 751 Molnar, C., Casalicchio, G., Bischl, B., 2020. Interpretable Machine Learning – A Brief History, State-of-the-Art
752 and Challenges. *Commun. Comput. Inf. Sci.* 1323, 417–431. https://doi.org/10.1007/978-3-030-65965-3_28
- 753 Morawska, L., Thai, P.K., Liu, X., Asumadu-Sakyi, A., Ayoko, G., Bartonova, A., Bedini, A., Chai, F.,
754 Christensen, B., Dunbabin, M., Gao, J., Hagler, G.S.W., Jayaratne, R., Kumar, P., Lau, A.K.H., Louie,
755 P.K.K., Mazaheri, M., Ning, Z., Motta, N., Mullins, B., Rahman, M.M., Ristovski, Z., Shafiei, M.,
756 Tjondronegoro, D., Westerdahl, D., Williams, R., 2018. Applications of low-cost sensing technologies for
757 air quality monitoring and exposure assessment: How far have they gone? *Environ. Int.*
758 <https://doi.org/10.1016/j.envint.2018.04.018>
- 759 Nair, D.J., Gilles, F., Chand, S., Saxena, N., Dixit, V., 2019. Characterizing multicity urban traffic conditions using
760 crowdsourced data. *PLoS One* 14, e0212845. <https://doi.org/10.1371/journal.pone.0212845>
- 761 O’Keeffe, K.P., Anjomshoa, A., Strogatz, S.H., Santi, P., Ratti, C., 2019. Quantifying the sensing power of
762 vehicle fleets. *Proc. Natl. Acad. Sci.* 116, 12752–12757. <https://doi.org/10.1073/PNAS.1821667116>
- 763 Pak, U., Ma, J., Ryu, U., Ryom, K., Juhyok, U., Pak, K., Pak, C., 2020. Deep learning-based PM2.5 prediction
764 considering the spatiotemporal correlations: A case study of Beijing, China. *Sci. Total Environ.* 699, 133561.
765 <https://doi.org/10.1016/J.SCITOTENV.2019.07.367>
- 766 Poggio, T., Banburski, A., Liao, Q., 2020. Theoretical issues in deep networks. *Proc. Natl. Acad. Sci. U. S. A.* 117,
767 30039–30045. [https://doi.org/10.1073/PNAS.1907369117/ASSET/286D1BEF-AF8A-4102-8819-
768 89571C3A6F11/ASSETS/IMAGES/LARGE/PNAS.1907369117FIG03.JPG](https://doi.org/10.1073/PNAS.1907369117/ASSET/286D1BEF-AF8A-4102-8819-89571C3A6F11/ASSETS/IMAGES/LARGE/PNAS.1907369117FIG03.JPG)
- 769 Reichstein, M., Camps-Valls, G., Stevens, B., Jung, M., Denzler, J., Carvalhais, N., Prabhat, 2019. Deep learning
770 and process understanding for data-driven Earth system science. *Nat.* 2019 5667743 566, 195–204.
771 <https://doi.org/10.1038/s41586-019-0912-1>
- 772 Ren, X., Mi, Z., Georgopoulos, P.G., 2020. Comparison of Machine Learning and Land Use Regression for fine
773 scale spatiotemporal estimation of ambient air pollution: Modeling ozone concentrations across the
774 contiguous United States. *Environ. Int.* 142, 105827. <https://doi.org/10.1016/J.ENVINT.2020.105827>
- 775 Shi, Y., Ka-Lun Lau, K., Ng, E., 2016. Developing Street-Level PM2.5 and PM10 Land Use Regression Models
776 in High-Density Hong Kong with Urban Morphological Factors. *Environ. Sci. & Technol.* 50, 8178–

777 8187. <https://doi.org/10.1021/acs.est.6b01807>

778 Shtein, A., Kloog, I., Schwartz, J., Silibello, C., Michelozzi, P., Gariazzo, C., Viegi, G., Forastiere, F., Karnieli,
779 A., Just, A.C., Stafoggia, M., 2019. Estimating Daily PM_{2.5} and PM₁₀ over Italy Using an Ensemble Model.
780 *Environ. Sci. Technol.* <https://doi.org/10.1021/acs.est.9b04279>

781 Su, J.G., Apte, J.S., Lipsitt, J., Garcia-Gonzales, D.A., Beckerman, B.S., de Nazelle, A., Texcalac-Sangrador, J.L.,
782 Jerrett, M., 2015. Populations potentially exposed to traffic-related air pollution in seven world cities.
783 *Environ. Int.* 78, 82–89. <https://doi.org/10.1016/j.envint.2014.12.007>

784 Su, J.G., Jerrett, M., Beckerman, B., 2009. A distance-decay variable selection strategy for land use regression
785 modeling of ambient air pollution exposures. *Sci. Total Environ.* 407, 3890–3898.
786 <https://doi.org/10.1016/J.SCITOTENV.2009.01.061>

787 Tang, R., Blangiardo, M., Gulliver, J., 2013. Using building heights and street configuration to enhance intraurban
788 PM₁₀, NO_x, and NO₂ land use regression models. *Environ. Sci. Technol.* 47, 11643–11650.
789 https://doi.org/10.1021/ES402156G/SUPPL_FILE/ES402156G_SI_001.PDF

790 Thompson, J.E., 2016. Crowd-sourced air quality studies: A review of the literature & portable sensors.
791 *Trends Environ. Anal. Chem.* 11, 23–34. <https://doi.org/10.1016/j.teac.2016.06.001>

792 Wang, A., Paul, S., deSouza, P., Machida, Y., Mora, S., Duarte, F., Ratti, C., 2023. Key Themes, Trends, and
793 Drivers of Mobile Ambient Air Quality Monitoring: A Systematic Review and Meta-Analysis. *Environ. Sci.*
794 *Technol.* <https://doi.org/10.1021/acs.est.2c06310>

795 Wang, H., He, X., Liang, X., Choma, E.F., Liu, Y., Shan, L., Zheng, H., Zhang, S., Nielsen, C.P., Wang, S., Wu,
796 Y., Evans, J.S., 2020. Health benefits of on-road transportation pollution control programs in China. *Proc.*
797 *Natl. Acad. Sci. U. S. A.* 117, 25370–25377.
798 https://doi.org/10.1073/PNAS.1921271117/SUPPL_FILE/PNAS.1921271117.SD01.XLSX

799 Wei, P., Brimblecombe, P., Yang, F., Anand, A., Xing, Y., Sun, L., Sun, Y., Chu, M., Ning, Z., 2021.
800 Determination of local traffic emission and non-local background source contribution to on-road air
801 pollution using fixed-route mobile air sensor network. *Environ. Pollut.* 290, 118055.
802 <https://doi.org/10.1016/J.ENVPOL.2021.118055>

803 Weissert, L.F., Salmond, J.A., Miskell, G., Alavi-Shoshtari, M., Williams, D.E., 2018. Development of a
804 microscale land use regression model for predicting NO₂ concentrations at a heavily trafficked suburban area
805 in Auckland, NZ. *Sci. Total Environ.* 619–620, 112–119. <https://doi.org/10.1016/j.scitotenv.2017.11.028>

806 World Health Organization, 2016. Ambient Air Pollution: A global assessment of exposure and burden of disease,
807 World Health Organization.

808 Xiao, Q., Chang, H.H., Geng, G., Liu, Y., 2018. An Ensemble Machine-Learning Model To Predict Historical
809 PM_{2.5} Concentrations in China from Satellite Data. *Environ. Sci. Technol.*
810 <https://doi.org/10.1021/acs.est.8b02917>

811 Yan, X., Zang, Z., Luo, N., Jiang, Y., Li, Z., 2020. New interpretable deep learning model to monitor real-time
812 PM2.5 concentrations from satellite data. *Environ. Int.* 144, 106060.
813 <https://doi.org/10.1016/J.ENVINT.2020.106060>

814 Zalzal, J., Alameddine, I., El Khoury, C., Minet, L., Shekarrizfard, M., Weichenthal, S., Hatzopoulou, M., 2019.
815 Assessing the transferability of landuse regression models for ultrafine particles across two Canadian cities.
816 *Sci. Total Environ.* 662, 722–734. <https://doi.org/10.1016/J.SCITOTENV.2019.01.123>

817 Zhao, H., Shi, J., Qi, X., Wang, X., Jia, J., 2017. Pyramid scene parsing network, in: *Proceedings - 30th IEEE*
818 *Conference on Computer Vision and Pattern Recognition, CVPR 2017.*
819 <https://doi.org/10.1109/CVPR.2017.660>

820 Zhong, S., Zhang, K., Bagheri, M., Burken, J.G., Gu, A., Li, B., Ma, X., Marrone, B.L., Ren, Z.J., Schrier, J., Shi,
821 W., Tan, H., Wang, T., Wang, X., Wong, B.M., Xiao, X., Yu, X., Zhu, J.J., Zhang, H., 2021. Machine
822 Learning: New Ideas and Tools in Environmental Science and Engineering. *Environ. Sci. Technol.* 55,
823 12741–12754. <https://doi.org/10.1021/ACS.EST.1C01339>

824 Zhou, Z., Lin, A., Wang, L., Qin, W., Zhao, L., Sun, S., Zhong, Y., He, L., Chen, F., 2021. Estimation of the losses
825 in potential concentrated solar thermal power electricity production due to air pollution in China. *Sci. Total*
826 *Environ.* 784, 147214. <https://doi.org/10.1016/J.SCITOTENV.2021.147214>

827 Zhou, Z.H., Feng, J., 2019. Deep forest. *Natl. Sci. Rev.* 6, 74–86. <https://doi.org/10.1093/NSR/NWY108>

828 Zhu, X., Zhang, Q., Du, X., Jiang, Y., Niu, Y., Wei, Y., Zhang, Y., Chillrud, S.N., Liang, D., Li, H., Chen, R.,
829 Kan, H., Cai, J., 2023. Respiratory Effects of Traffic-Related Air Pollution: A Randomized, Crossover
830 Analysis of Lung Function, Airway Metabolome, and Biomarkers of Airway Injury. *Environ. Health*
831 *Perspect.* 131. <https://doi.org/10.1289/EHP11139>

832